Magnetic Resonance in Medicine 75:1935–1948 (2016)

Interleaved Multishot Imaging by Spatiotemporal Encoding: A Fast, Self-Referenced Method for High-Definition Diffusion and Functional MRI

Rita Schmidt, Amir Seginer, and Lucio Frydman*

Purpose: Single-shot imaging by spatiotemporal encoding (SPEN) can provide higher immunity to artifacts than its echo planar imaging–based counterparts. Further improvements in resolution and signal-to-noise ratio could be made by rescinding the sequence's single-scan nature. To explore this option, an interleaved SPEN version was developed that was capable of delivering optimized images due to its use of a referenceless correction algorithm.

Methods: A characteristic element of SPEN encoding is the absence of aliasing when its signals are undersampled along the low-bandwidth dimension. This feature was exploited in this study to segment a SPEN experiment into a number of interleaved shots whose inaccuracies were automatically compared and corrected as part of a navigator-free image reconstruction analysis. This could account for normal phase noises, as well as for object motions during the signal collection.

Results: The ensuing interleaved SPEN method was applied to phantoms and human volunteers and delivered high-quality images even in inhomogeneous or mobile environments. Submillimeter functional MRI activation maps confined to gray matter regions as well as submillimeter diffusion coefficient maps of human brains were obtained.

Conclusion: We have developed an interleaved SPEN approach for the acquisition of high-definition images that promises a wider range of functional and diffusion MRI applications even in challenging environments. **Magn Reson Med 75:1935–1948, 2016. © 2015 Wiley Periodicals, Inc.**

Key words: spatiotemporal encoding; interleaved MRI; high-definition fMRI; high-resolution ADCs; full refocusing; referenceless reconstruction

INTRODUCTION

Single-scan MRI techniques play important roles in functional, diffusion, flow, thermometry, and real-time anatomical studies. A key component of many of these subsecond applications is echo planar imaging (EPI) (1–6). One of EPI's drawbacks stems from its sensitivity to field and shift inhomogeneities along the low-bandwidth direction (7). Recent studies have focused on alternative single-scan methods derived from spatiotemporal encoding (SPEN) (8), a strategy that combines frequency-swept pulses and gradients to image this dimension (9). SPEN offers the possibility of using stronger acquisition gradients than those used in EPI, resulting in a higher immunity to field inhomogeneities (10,11). An important feature of SPEN is its ability to scan the low-bandwidth dimension under "fully refocused" conditions, whereby each excited spin packet experiences a full spin echo at the time of its sequential detection (12). This further increases the robustness of the scan to various sources of offset. A variety of sequences combining hybrid *k*- and SPEN-space encoding along the high- and low-bandwidth dimensions have thus been demonstrated, with advantageous results for functional, diffusion, anatomic, and thermometry applications (13–17).

Despite this potential, single-scan SPEN images may still suffer from blurring, signal loss, and distortions. This degradation will occur, as in EPI, due to the long acquisition durations imposed by gradient slew rates and gradient strength limitations, particularly in clinical scanners. To reduce these long acquisition times, we explored an interleaved multishot sequence using principles akin to those employed in interleaved EPI (18,19). Well-known weaknesses of multishot interleaved EPI include the appearance of ghosts and blurring resulting from phase errors between shots (20,21), instrumental instabilities, respiration and cardiac pulsations, or other bulk motions (22–25). Accounting for these phase errors requires the acquisition of ancillary navigator scans or even more complex forms of reference scan acquisition (26,27). Although correction methods for interleaved EPI involving no reference scans have also been proposed (28,29), such implementations are not always applicable. The proposed interleaved multishot SPEN approach possesses a valuable advantage with regard to these methods, as it can deliver an improved image free from artifacts via a referenceless reconstruction procedure. This benefit results from SPEN's non-Fourier nature and from its lack of image aliasing artifacts upon attempting to reconstruct images from sparsely sampled data. This advantage (30) has no counterpart in EPI and, as shown in this study, can correct errors stemming from the aforementioned instrumental and in vivo instabilities. The outcome is a new approach to interleaved multishot SPEN that can provide robust high-resolution images. We explored this approach using phantom studies and human volunteer studies, including brain functional MRI (fMRI) and diffusion experiments, multislice breast

---

Chemical Physics Department, Weizmann Institute of Science, Rehovot, Israel

Grant sponsor: Israel Ministry of Trade and Industry; Grant number: Kamin-Yeda Project 711237; Grant sponsor: European Research Council; Grant number: 246754; Grant sponsor: Federal German Ministry for Education and Research; Grant number: DIP Collaborative Project 710907; Grant sponsor: Helen and Martin Kimmel Award for Innovative Investigation; Grant sponsor: Perlman Family Foundation.

*Correspondence to: Lucio Frydman, Chemical Physics Department, Weizmann Institute, 76100 Rehovot, Israel. E-mail: lucio.frydman@weizmann.ac.il

Received 16 July 2014; revised 31 March 2015; accepted 31 March 2015
DOI 10.1002/mrm.25742

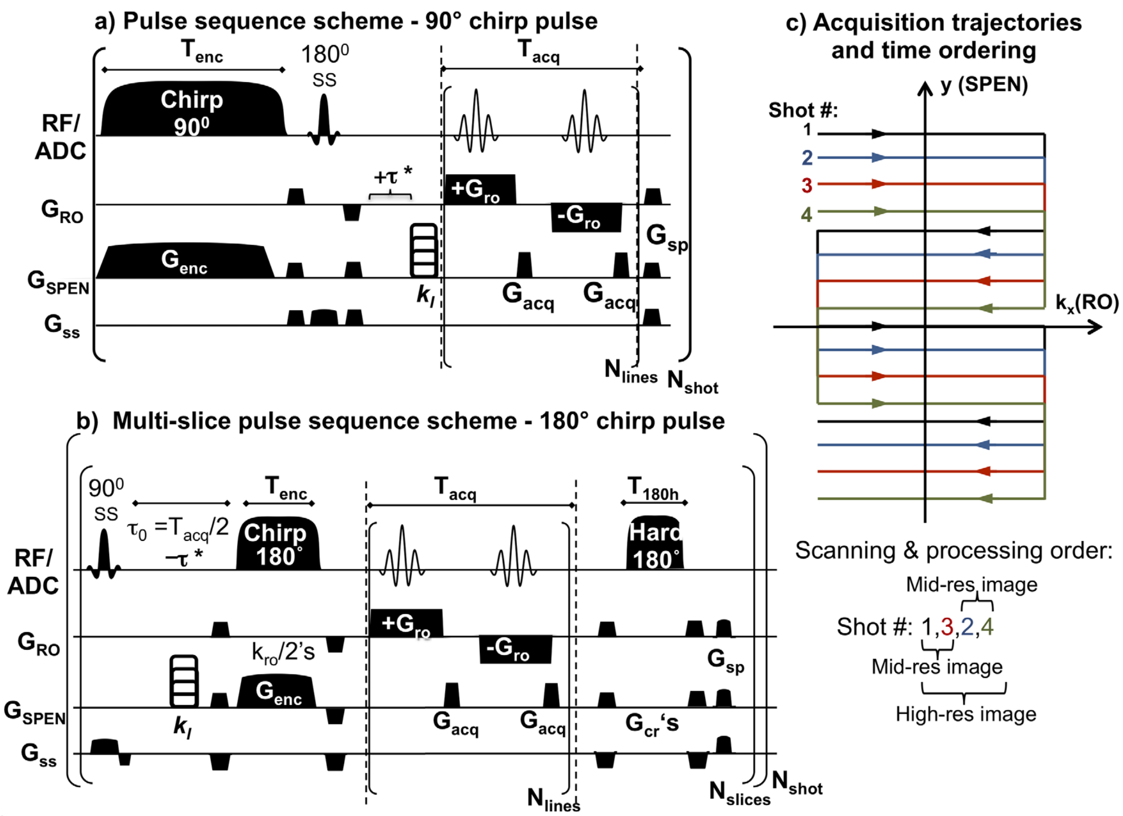

* For sensitizing the sequences to BOLD effects, scans were collected by adding the τ delay as indicated (see text for further details)

FIG. 1. Interleaved multishot SPEN pulse sequence schemes. (**a**) 90 deg chirp pulse sequence involving a central slice-selective (ss) spin echo. (**b**) Multislice interleaved SPEN version using an initial 90 deg slice-selective excitation, a pre-encoding delay τ_o (tuned to fully refocused conditions as an example), a 180 deg chirp pulse, and a postacquisition hard 180 deg pulse returning all spins outside the targeted slice back to thermal equilibrium. (**c**) Acquisition trajectory in the hybrid SPEN/readout space for a four-shot interleaved acquisition case, with a pair of two-shot intermediate reconstruction. When implementing functional MRI scans, uniform delays τ were introduced as illustrated in the sequences. If the BOLD-sensitizing delay τ is desired $>T_{acq}/2$, τ_o is set to 0 and a delay $\tau - \mathrm{T}_{acq}/2$ is added after the 180 deg chirp pulse. Abbreviations: cr, crusher; RF/ADC, radiofrequency and analog-to-digital conversion channels; RO, readout; sp, spoiler

imaging studies, and studies wherein volunteers were asked to move between shots.

THEORY

Pulse Sequence Considerations

For the sake of simplicity, we consider first the execution of a one-dimensional (1D) SPEN experiment along the y-axis. SPEN delivers its images by the combined action of a chirp pulse of rate R and duration T_{enc}, and of a gradient of strength G_{enc} (31,32). These parameters are related to the experiment's field of view (FOV) through $BW = RT_{enc} = \gamma G_{enc} FOV$, where BW is the chirp pulse bandwidth. Such combination imparts a parabolic phase profile on the encoded spins $\varphi_{enc}(y) = \alpha_{enc} y^2 + \beta_{enc} y + const$. For SPEN experiments based on 90 deg excitation chirp pulses (Fig. 1a) $\alpha_{90^\circ} = -\frac{\gamma G_{enc} T_{enc}}{2FOV}$, $\beta_{90^\circ} = \frac{\gamma G_{enc} T_{enc}}{2} - \frac{w_{cs} T_{enc}}{FOV}$; if SPEN is based on 180 deg adiabatic sweeps (Fig. 1b), then $\alpha_{180^\circ} = -\frac{\gamma G_{enc} T_{enc}}{FOV}$, $\beta_{180^\circ} = \gamma G_{enc} T_{enc} - \frac{w_{cs} T_{enc}}{FOV}$, with β_{180° including a prephasing gradient and w_{cs} the frequency offset.

The signal acquired in a 1D SPEN MRI experiment can be expressed as (11)

$$S(t) = \int_{-\frac{FOV}{2}}^{\frac{FOV}{2}} \rho(y) e^{i[\varphi_{enc}(y) + k(t)y]} dy, \qquad [1]$$

where $k(t) = \gamma \int_0^t G_{acq}(t')dt'$ describes the effects of a gradient applied during the acquisition. It has been shown based on the stationary phase approximation that this signal will be proportional to the spin density profile $\rho(y)$. Image reconstruction, however, is enhanced by super-resolution (SR) methods (33–35) that improve resolution and allow one to use lower R rates and lower gradient strengths, thereby decreasing the overall specific absorption rate (SAR). In the SR method implemented in this study, the integral in Equation [1] is replaced by an expression that assumes N discrete spatial points $\{\rho_n\}_{\mathrm{n=1...N}}$ and M discrete measured points $\{S_m\}_{\mathrm{m=1...M}}$, leading to

$$S(k_m) \approx \sum_{n=1}^{N} \rho_n \int_{y_n-\delta}^{y_n+\delta} e^{i[\alpha_{enc} y^2 + (\beta_{enc} + k_m)y]} dy = \sum_{n=1}^{N} \rho_n A_{mn}, \qquad [2]$$

where y_n is the voxel's y center, 2δ is the voxel's width, and A_{mn} are elements of a so-called SR matrix. Equation

[2] can be rewritten in matrix form as $S = A\rho$; the image retrieval problem can then be solved in the $N \leq M$ case as $\rho = A^{(-1)}S$ where $A^{(-1)}$ is a matrix required for a stable solution. As in previous studies, we used a single-iteration algorithm based on the conjugate gradient method to find this matrix and solve for ρ, including a Gaussian weighting of A's columns before the calculation of this inverse matrix (30,33).

These 1D principles can be extended to a single-scan two-dimensional (2D) imaging setting by considering a hybrid SPEN sequence (9–11) that combines a k-space acquisition in the readout direction, with SPEN in the low-bandwidth direction. In this case, the final spin density will be a matrix ρ_{nq}, where $n = 1\ldots N$ indexes the points along the SPEN dimension and $q = 1\ldots Q$ denotes points in the readout direction (Fig. 1). As happens for EPI (19), this single-shot sequence can be further extended into an interleaved multishot format endowed with a higher definition, better sensitivity, and improved robustness against frequency offsets along the low-bandwidth dimension (20). In the EPI case, interleaved acquisitions are compromised by a need for corecording ancillary calibrating scans for their processing, thus avoiding increased Fourier artifacts. SPEN methods circumvent this penalty due to their avoidance of Fourier processing along the low-bandwidth dimension. To appreciate this feature, consider a multishot SPEN experiment entailing a repeat of N_{shot} interleaved scans that differ by the addition—prior to their respective acquisitions—of a proper gradient-driven displacement along their low-bandwidth directions. Figure 1c presents the fashion in which this multishot array can be reconstructed into a unified data set for $N_{shot} = 4$. Assuming that each one of these N_{shot} acquisitions entails M points along their SPEN axes, the result will be an array of SPEN data sets composed of $M_{total} = M\text{x}N_{shot}$ points. Each SPEN shot will now involve a larger blipped gradient of area $\Delta k_{acq} = \frac{\lambda_{enc} \cdot \gamma G_{enc} T_{enc}}{M_{total}/N_{shot}}$ and be preceded by a variable "k-kick" $k_l = \frac{\lambda_{enc} \cdot \gamma G_{enc} T_{enc}}{M_{total}}(l-1)$ $(l = 1\ldots N_{shot})$, where λ_{enc} depends on whether the encoding was implemented by a 90 deg or 180 deg frequency sweep: $\lambda_{90^\circ} = 1$ and $\lambda_{180^\circ} = 2$. The interleaved data rearrangement described in Figure 1c thus gives sufficient information to reconstruct the spin density from these M points, even if each scan's acquisition time was reduced by N_{shot} and concurrently shorter pulse durations were required for achieving the fully refocused conditions $T_{acq} = \lambda_{enc} T_{enc}$ (13,36).

Referenceless Reconstruction of Interleaved SPEN Data

In contrast to EPI, where $\Delta k = \frac{2\pi}{FOV}$, the SPEN Δk_{acq} just introduced is proportional to the FOV. This follows from the stationary phase approximation and from Equation [1]: $\Delta k_{acq} = -2\alpha_{enc}\frac{FOV}{M}$. Hence, if one compares an EPI experiment in which k-space data set is undersampled by a factor of N_{shot} with regard to a comparable SPEN data acquisition, EPI's Δk step increase will result in a reduction of the image's FOV to FOV/N_{shot} and produce an aliasing effect. In contrast, a similar step increase in SPEN will keep the FOV constant but increase the sampling intervals of the stationary point (i.e., reduce the image's resolution). In other words, interleaved SPEN allows one to shorten each scan's duration at the expense of decreasing spatial resolutions, but not at the cost of aliasing. A four-shot interleaved SPEN acquisition, for instance, could have the data from each shot reconstructed separately to yield images with the same FOV as a full SPEN acquisition but with spatial resolutions reduced by a factor of four. Moreover, pairs of scans in this {1,2,3,4} series could be jointly coprocessed as {1,3} and {2,4} (Fig. 1c) to yield two midresolution images with double the spatial resolution, and an image with maximum resolution could be reconstructed by coprocessing all four shots. This hierarchical reconstruction can be further extended in a "sliding window" fashion (Fig. 2) to yield high-definition images without paying the full temporal acquisition penalty.

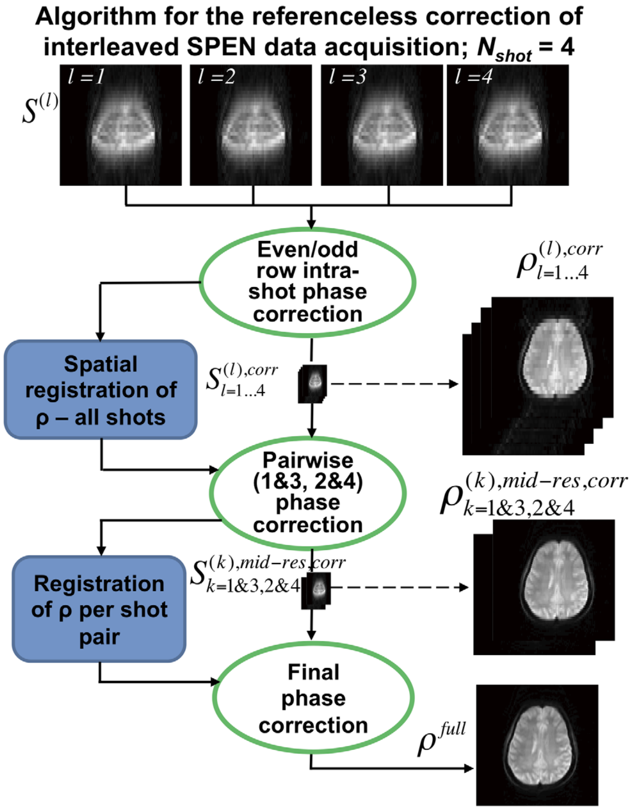

FIG. 2. Referenceless processing algorithm for the reconstruction of interleaved multishot SPEN data with corrections for the phase errors and motions exemplified for an experimental four-shot acquisition case. The relationships between the various signal and spin density S- and ρ-matrices are further described in the text; in the present example, all of these matrices are presented after Fourier transformation along the readout direction, and processes indicate actions taken along the SPEN dimension.

Absence of aliasing in undersampled SPEN images enables a referenceless joint reconstruction of all scans based on an estimation of the phase errors among the interleaved data. The principle of referenceless SPEN reconstruction was demonstrated for the coprocessing of single-scan even-and-odd data sets via a common SR procedure (30); in this study, we adopted and extended these principles to the coreconstruction of multiple interleaved SPEN acquisitions without ancillary navigators. Toward this end the signal of each shot, $\{S^{(l)}\}_{l=1,N_{shot}}$ is used to reconstruct a low-resolution image $\{\rho_{nq}^{(l)} = [A_{mn}^{(l)}]^{-1} S_{mq}^{(l)}\}_{l=1,N_{shot}}$, where $n = 1 \ldots N/N_{shot}$ and $m = 1 \ldots M = M_{total}/N_{shot}$ index the points along SPEN's image and digitized dimensions, and $q = 1 \ldots Q$ are points along the readout direction. Here, $A_{mn}^{(l)}$ represents the pertinent SR matrix for shot l (including the relevant k_l shifts for each of the shots), defined similarly as in Equation [2] by

$$A_{mn}^{(l)} = \int_{y_n-\delta}^{y_n+\delta} e^{i\left[\alpha_{enc}y^2+\left(\beta_{enc}+k_l+\Delta k_{acq}\cdot(m-1)\right)\right]} dy. \quad [3]$$

In an ideal case, one would expect to obtain nearly identical $\{\rho_{nq}^{(l)}\}_{l=1,N_{shot}}$ low-resolution images for all the scans involved in the multishot acquisition. However, due to intermittent errors between shots, phases will be added to the solutions, and $\rho_{nq}^{(l)}$ reconstructed from the various shots will differ. To estimate these phase errors and achieve a consistent set of data, we correct each shot's low-resolution images as

$$\frac{\rho_{nq}^{(l)}}{\rho_{nq}^{(l=1)}} = e^{i\phi_{nq}}, \rho_{nq}^{(l),corr} = e^{-i\phi_{nq}} \rho_{nq}^{(l)}. \quad [4]$$

The justification for this correction is as described by Seginer et al. (30) for the referenceless coprocessing of even/odd lines in single-shot SPEN acquisitions. As in the study by Seginer et al., it is practical to generate the phase maps φ_{nq} corresponding to each of these images as a general 2D fit of the experimental phase differences based on a second-order polynomial expansion. With the corresponding correction applied to all images, a set of undersampled signals $S^{(l)corr} = A_{mn}^{(l)} \rho_{nq}^{(l)corr}$ (where in fact $S^{(1),corr} = S^{(1)}$) is back calculated. Sampled data points thus corrected can be combined again in an interleaved fashion as

$$S^{corr} = \begin{bmatrix} S_{1,1}^{(l=1),corr} & \cdots & S_{1,Q}^{(l=1),corr} \\ S_{1,1}^{(l=2),corr} & \cdots & S_{1,Q}^{(l=2),corr} \\ \vdots & & \\ S_{1,1}^{(l=N_{shots}),corr} & \cdots & S_{1,Q}^{(l=N_{shots}),corr} \\ \vdots & & \\ S_{M_{total}/N_{shots},1}^{(l=1),corr} & \cdots & S_{M_{total}/N_{shots},Q}^{(l=2),corr} \\ S_{M_{total}/N_{shots},1}^{(l=2),corr} & \cdots & S_{M_{total}/N_{shots},Q}^{(l=2),corr} \\ \vdots & & \\ S_{M_{total}/N_{shots},1}^{(l=N_{shots}),corr} & \cdots & S_{M_{total}/N_{shots},Q}^{(l=N_{shots}),corr} \end{bmatrix}. \quad [5]$$

Coprocessing of this augmented matrix then yields a high-resolution image ρ_{nq}^{full} from $\rho_{nq}^{full} = [A_{mn}^{full}]^{-1} S_{mq}^{corr}$, with n, q, and m as before. Although theoretically this procedure should be sufficient, we found that, in practice, possible inaccuracies arising from the small number of image points collected in each shot make it suboptimal. To improve the SR solution's stability, we perform the $\{\rho_{nq}^{l} = [A_{mn}^{(l)}]^{-1} S_{mq}^{(l)}\}_{l=1,N_{shot}}$ inversion in an iterative loop, each time combining a pair of images to generate progressively higher levels of resolution. For example, in the four-shot case (Fig. 2), one would first coprocess shot 1 with shot 3 and shot 2 with shot 4 to correct for the phase error within each pair, generating a pair of midresolution images. The phase-balancing procedure would then be repeated for these two midresolved images to correct for the phase error between them; this set of images is then jointly coprocessed to obtain the final, highest-resolution image. With such a procedure, the number of points participating in the phase error correction becomes higher as the iteration number increases, improving the correction's accuracy. For the case where the number of shots is a power of two (ie, $N_{shot} = 2^p$), the total number of iterations is thus $p + 1$, including a first iteration that corrects the even/odd phase errors within each shot (e.g., for four interleaves, the number of iterations would be three).

A potentially important source of artifacts in segmented acquisitions stems from movements in the imaged object. In k-encoded methods like EPI, motion leads to phase errors between the various images, primarily along the phase-encoded direction. In SPEN, one can use the previously mentioned absence of aliasing effects to correct common cases of in-plane rigid motions without the use of ancillary navigators. The solution of each shot's equation $\rho_{nq}^{(l)} = [A_{mn}^{(l)}]^{-1} S^{(l)}$ would then deliver low-resolution images of the shifted object; these can be coregistered, for instance by applying canonical rotation ($\hat{R}$) and translation ($\overrightarrow{R}_0$) transformations: $\rho_{nq}^{(l),registered}(\overrightarrow{r}_{nq}) = \rho_{nq}^{(l)}(\hat{R}\overrightarrow{r}_{nq} + \overrightarrow{R}_0)$ (22). With these corrections, it becomes possible to recalculate back images of the targeted object in a common, "static" frame, $S^{(l),registered} = A_{mn}^{(l)} \rho_{nq}^{(l),registered}$ Once individual images are coregistered, the previously described phase error correction procedure can be used again. The effect of the rotation and translation transformations will result in in-plane, spatially dependent phase shifts that in all likelihood will be different from the initial phase error terms. These new terms will still be fully compatible with an in-plane 2D phase correction of the kind shown in Figure 2; the additional coregistration procedure can thus be added as intermediate step between the previously described phase correction iterations.

Signal-to-Noise Ratio Considerations

Before discussing signal-to-noise ratio (SNR) in the case of multishot SPEN, we briefly recapitulate the main SNR features of single-shot SPEN with regard to single-shot EPI. As originally shown by Tal and Frydman (12), SPEN's SNR is $1/\sqrt{N}$ times lower than that of k-space encoded MRI if pulse parameters are chosen so that a magnitude calculation of the SPEN signal will represent the spin density with identical range and resolution—a kind of SPEN acquisition that demands $\lambda_{enc} BW \cdot T_{enc} = N^2$ (in this case, $N = M$). However, SR reconstruction algorithms allow one to choose lower encoding *BW* bandwidths without sacrificing resolution, thereby improving SPEN's SNR. In such cases, and as discussed in detail by Ben-Eliezer et al. (37), the ratio between the SNR of SPEN and of EPI acquisitions will become $\sqrt{\frac{M}{\lambda_{enc} BW \cdot T_{enc}}}$ as illustrated analytically and with numerical simulations, this ratio can be made virtually unity for suitably set single-shot acquisitions. With regard to multishot acquisitions, as happens to be the case when executing EPI in an interleaved fashion, interleaved SPEN exhibits an improved per-scan SNR when compared with averaged single-shot counterparts with the same final spatial resolution. Taking into account T_2 weightings and using a notation similar to that described by Ben-Eliezer et al., the SNR can be summarized for interleaved SPEN as $\Delta y \Delta x \sqrt{\frac{QN}{sw}} \sqrt{\frac{M_{total}}{\lambda_{enc} BW \cdot T_{enc}}} \cdot e^{-TE_m/T_2}$. Here, *sw* is the readout spectral width, Δx and Δy are the final spatial resolutions along the read-out and SPEN directions, Q and N are the total number of points acquired along the readout and spatiotemporal encoding directions, $BW \cdot T_{enc}$ is the time-bandwidth product of the chirp pulse, and $\lambda_{enc} = 1$ or 2 as introduced above. Similar to the single-shot case, the $\sqrt{\frac{M_{total}}{\lambda_{enc} BW \cdot T_{enc}}}$ ratio reflects SPEN's generally lower SNR versus EPI due to its direct (as opposed to reciprocal) space sampling nature (12,37). The TE_m mentioned in the SPEN SNR expression is the echo time (TE) for each of the acquired points, which falls in the $0 < TE_m < 2T_{acq}$ range for the 90 deg chirp pulse sequence and in $T_{acq}/2 \leq TE_m \leq 2T_{acq}$ for the 180 deg chirp pulse sequence (with both cases assumed recorded under fully refocused conditions). Because acquiring a high-resolution image within a single-shot requires longer T_{enc} and TE_m times compared with the values needed for an interleaved counterpart, this expression predicts that the SNR improvements brought about by interleaving can be substantial. As in interleaved EPI methods, this shortening in the encoding and acquisition times may also enable one to reduce the repetition time (TR). Although this was not done in our phantom-based SNR comparisons, should the TR be shortened, then potential saturation effects or the possibility of changing the optimized excitation angle should be factored into the SNR considerations (38). The Appendix describes some of these TE- and TR-related SNR effects as calculated for a set of prototypical T_1 and T_2 values. These calculations reveal that the SNR gain achievable by multishot acquisitions due to shorter TEs can be substantial; for example, four-shot SPEN images collected over a total scan time of 3 s (ie, TR = 0.75 s) using a TE range of 40–100 ms could yield SNR improvements ranging between 1 and 10 depending on location and the exact relaxation parameters assumed, despite the fact that resolution is being improved by a factor of 4. Moreover, the shortened encoding/acquisition times also increase immunity against B_0 inhomogeneity, leading to a dramatic potential to improve an image's quality (e.g., see Fig. 4).

METHODS

The principles just described were explored with a series of phantom tests aimed at examining the benefits that the interleaved procedure could deliver in relatively inhomogeneous B_0 environments as well as in the presence of motions. The phase and motion correction algorithms were also explored in vivo on healthy volunteers, including high-definition fMRI studies of a motor paradigm and diffusion-weighted brain sagittal studies. All these experiments were implemented on a 3T Siemens TIM TRIO scanner (Siemens Healthcare, Erlangen: Germany) using custom-written codes based on the sequences in Figures 1a and 1b. The ensuing images were reconstructed using custom-written MATLAB packages (MathWorks, Natick, Massachusetts, USA) that included the rearrangements and the algorithms described in Figure 2, as well as Fourier transformation along the *k*-space readout direction. (The acquisition and reconstruction codes are available upon request.)

One set of experiments was performed using an American College of Radiology MRI phantom to demonstrate the SNR and resolution improvement arising from interleaved SPEN acquisitions. Another set of phantom experiments was conducted to examine the performance of interleaved SPEN and EPI acquisitions in inhomogeneous B_0 environments using an orange and banana setup as an example.

Human volunteer imaging studies were approved by the Internal Review Board of the Wolfson Medical Center (Holon, Israel) and were performed after obtaining informed consent. One such set of experiments centered on fMRI brain scans using a four-channel head coil with T_2^* weighting (ie, with SPEN's fully refocused conditions broken by the addition of a pre-acquisition delay τ), introducing a T_2^* weighting akin to that in gradient echo EPI (GE-EPI). The paradigm of these experiments was a motor stimulus involving the uninterrupted tapping of all fingers (tapping frequency of ~2 Hz) in either the right or the left hand for 30 s each (39); five pairs of such stimuli blocks were conducted for a total study duration of 5 min. The functional experiments were repeated using both single-shot GE-EPI and interleaved four-shot SPEN. The GE-EPI echo time as well as the equivalent delay responsible for the T_2^* weighting in the four-shot SPEN experiments were set to $\tau = 30$ ms. It is important to stress that in the case of SPEN, this delay breaks an otherwise fully refocused condition that would free signals from T_2^* effects. Therefore, τ yielded a position-independent BOLD weighting, without which no activation could be detected under the field and functional paradigms hereby assayed. In order to keep a constant scan time per (final) image, the TR of the four-shot SPEN was 0.75 s, and the flip angle was 60 deg. These experiments were repeated on four volunteers (three of whom underwent axial experiments and a fourth who underwent coronal experiments), and axial as well as coronal orientations were scanned. For deriving functional activation, t-score maps were calculated (40) for all the axially scanned volunteers, as statistical significance of the mean signal difference in a time series between two conditions in a voxel-by-voxel basis, using a gamma function to account for the hemodynamic response function (41). The average percent of signal changes over the time course of the stimuli were calculated for both SPEN and GE-EPI scans on identical regions chosen from the anatomical image on these subjects for GE-EPI and on SPEN experiments executed with a matrix of 128×260 pixels (128×130 pixels for one subject). The error bars for these activation plots reflect the standard error observed for the region of interest over the stimuli repetitions. These calculations were performed in MATLAB using custom-written software.

An additional set of interleaved SPEN brain experiments centered on diffusion-weighted scans (42) was collected in a sagittal orientation. Toward this end, the multislice sequence (Fig. 1b) was modified to include diffusion-weighting gradients. Mean ADCs were extracted from images generated from a single, two, and four interleaved shots after suitable calculations of the SPEN-weighted b values (43) arising from diffusion weightings applied along all orthogonal axes, with nominal b values ranging from 0 to 1000 s/mm^2. Comparisons against single-shot spin echo EPI (SE-EPI) were also made; interleaved SE-EPI acquisitions were not pursued due to poor performance. It is worth noting that in these in vivo diffusion-weighted experiments, a high phase-wrapping was detected, which required a careful phase unwrapping algorithm (44) to implement the referenceless procedure in Figure 2.

In addition to these brain studies, human breast images were collected using the sequence in Figure 1b in order to explore the performance of multislice interleaved SPEN when operating in heterogeneous tissue environments; these results can be found in Supporting Figure S1.

A final set of experiments involved examining the capability of the algorithm in Figure 2 to account for phase errors associated with rigid body motions. These experiments involved phantoms that were artificially moved along the SPEN direction and volunteers who were requested to swivel their heads in a right-to-left motion throughout the course of a brain scan. To find rigid transformations that best compensate for the motion, a minimization of the (absolute) correlations between intermediate images (after a rigid transformation) was performed using an open-source MATLAB code (45) relying on the *fminsearch* function and the Nelder-Mead algorithm (46). Low-resolution images thus registered were used as an input for the phase error correction algorithm as shown in Figure 2.

RESULTS

Interleaved SPEN: Phantom Experiments

Figure 3 shows representative results collected on an American College of Radiology phantom, comparing the SNR of images collected with the same final resolution using single-scan SPEN versus two- and four-shot interleaved examples. The SNR improvement with increasing number of shots is evident, with the sensitivity of the four-shot image is about four times higher than that of its single-shot counterpart. These gains derive from the considerably shorter echo times involved in the interleaved SPEN with regard to single-shot acquisitions: 32 ms for the four-shot SPEN versus 107 ms for the single-shot SPEN at the middle of the image. Such reduction leads to significant SNR gains, as T_2 tissue values are in the 60–120 ms range. An additional point to notice is the reduced T_2 weighting along the SPEN direction, when images are collected in multiple shots. Also illustrated in Figure 3 is the fact that if the same acquisition durations are used in the single-shot and multishot schemes, a higher resolution image will result from the latter due to the larger number of points acquired. Further resolution improvements can derive from exploiting SPEN's built-in restricted FOV features, which can be used in the interleaved implementation for improving the resolution even further. This is exemplified by the profiles in Figure 3h, which compares similar SPEN acquisitions collected with a full FOV and with half the FOV.

Figure 4 examines the robustness of interleaved multishot SPEN and EPI scans to B_0 inhomogeneity. The setup included a banana and an orange positioned in the central FOVs, and single versus interleaved shots were compared seeking morphological details at a 1–2 mm resolution. Although the single-shot SPEN image was considerably less distorted than its single-shot EPI counterpart, both failed to provide sufficient resolution—and in the case of the banana, which had a shorter T_2, signal intensity was similarly insufficient. Considerable improvements arose from acquiring four interleaved shots; still, even in this case, the EPI image showed higher distortions than its SPEN counterpart when compared with their multiscan reference. It is worth noting that the single-shot SPEN immunity to B_0 inhomogeneity could in principle be improved by increasing the chirped pulse bandwidth; such improvement, however, would come at the cost of increased SAR and reduced SNR. These compromises were alleviated upon operating in a multishot, interleaved acquisition mode.

High-Definition Functional Brain Examinations by Interleaved SPEN MRI

To further examine the potential of this method, fMRI measurements of motor stimuli were performed using single-scan SPEN and EPI, as well as interleaved SPEN. Figure 5 shows a summary of these measurements, with magnitude images reconstructed from single-shot GE-EPI (usually considered a gold standard in this type of experiment) and from interleaved four-shot SPEN sequences, displayed with an overlay of those pixels showing a t-score ≥ 5. These images clearly show that the four-shot acquisitions delivered a higher spatial resolution without penalties derived from a stronger T_2 or T_2^* weighting. The activation areas in these interleaved SPEN experiments (Fig. 5b,c) are similar to those in conventional GE-EPI. This performance is evidenced in both the axial and coronal acquisitions. Figure 5e shows the percentage of the signal change due to the stimuli in axial scans performed by GE-EPI and by interleaved SPEN. The latter shows an increase in the signal activation by ~50%; this illustrates the potential of the new method, even if further studies are needed to assess the precise factors contributing to such an enhancement.

It is enlightening to use this fMRI example to illustrate how the SPEN phase maps vary between individual shots, and how these are estimated and compensated using the new referenceless correction method. Phase maps from a representative fMRI experiment together

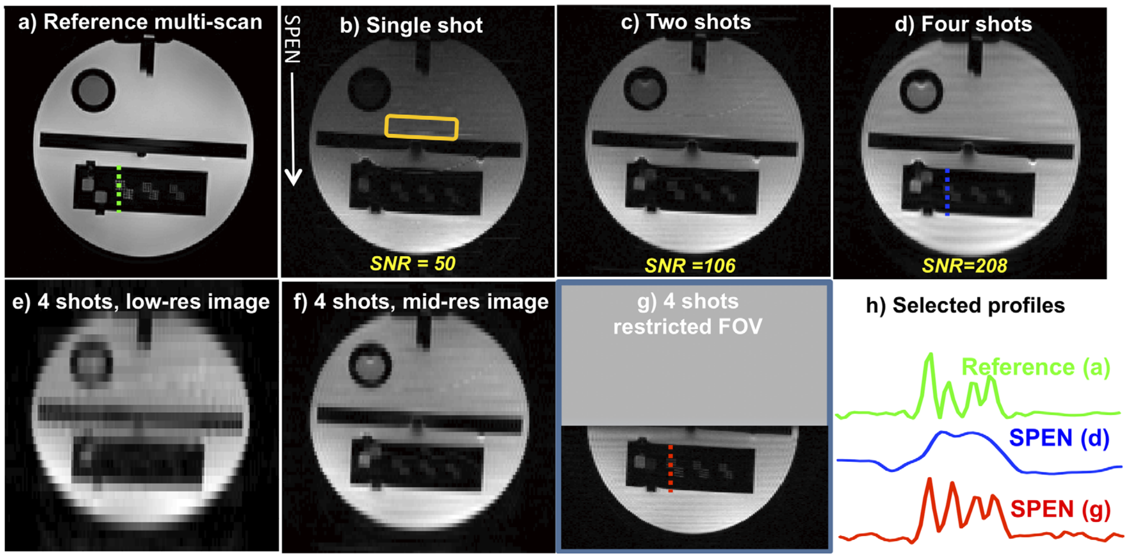

FIG. 3. Interleaved SPEN experiments collected on the American College of Radiology phantom. (**a**) Multiscan 2D profile of the phantom. (**b–d**) Single-shot (b), two-shot (c), and four-shot (d) SPEN scans collected with the same final resolution. The SNR displayed on these images was calculated by focusing on the yellow marked region; notice as well the decreased T_2 effects with increased interleaving. (**e, f, d**) Images reconstructed from a single shot (e), a pair of shots (f) and a four-shot acquisition leading to (d); all shots contained the same number of points, and the progression illustrates the process illustrated in Figure 2. (**g**) Interleaved four-shot SPEN image acquired as in (d), but with a restricted FOV leading to higher resolution. (**h**) Image profiles plotted along the segmented line marked on images (a), (d), and (g); the resolution achieved for the phantom's fine structure along this line can be seen to improve upon relying on the restricted FOV four-shot SPEN (see Methods for further parameters). Common scan parameters: sequence in Figure 1a, FOV $24 \times 24\,\text{cm}^2$, final resolution $1.7 \times 1.7\,\text{mm}^2$, slice thickness = 4 mm. Parameters for the four-shot SPEN were: flip angle = 60 deg, $T_{enc} = 25$ ms, $T_{acq} = 25$ ms, $G_{enc} = 0.06$ G/cm, TE = 7–57 ms (depending on the position of the spins), number of acquired points = 140 × 35 per shot, and TR = 0.75 s. Parameters for the two-shot SPEN were: flip angle = 60 deg, $T_{enc} = 50$ ms, $T_{acq} = 50$ ms, $G_{enc} = 0.06$ G/cm, TE = 7–107 ms, number of acquired points = 140 × 69 per shot, and TR = 0.75 s. Parameters for the single-shot SPEN were: flip angle = 90 deg, $T_{enc} = 100$ ms, $T_{acq} = 100$ ms, $G_{enc} = 0.05$ G/cm, TE = 7–207 ms, number of acquired points 140 × 140, and TR = 3 s. In addition a restricted FOV, four-shot SPEN scans were run with the same number of acquired points as for the full FOV, thus further increasing the resolution. This scan was run with the following parameters: FOV = $24 \times 12\,\text{cm}^2$, final resolution = $1.7 \times 0.85\,\text{mm}^2$, flip angle = 60 deg, $T_{enc} = 25$ ms, $T_{acq} = 25$ ms, $G_{enc} = 0.12$ G/cm, TE = 7–57 ms, the number of acquired points 140 × 35 per shot, and TR = 750 ms. Reference spin echo multiscan parameters were: resolution = $0.93 \times 0.93\,\text{mm}^2$, TE = 72 ms, TR = 1.5 s, number of scan averages = 2, and total scan duration = 35 s. The striated appearance on some of the images arises from the noniterative method that was chosen for the SR reconstruction and is not related to the use of scan interleaving. Alternative reconstruction methods (34,35) appear to be devoid of such minor artifacts.

with intermediate steps involved in processing interleaved scans into a final high-definition image can be found in Supporting Figure S2.

High-Definition Diffusion-Weighted MRI by Interleaved SPEN

In an additional exploratory study, interleaved diffusion-weighted SPEN images were recorded for a human brain along a sagittal orientation. All these images are compared for $b = 0$ in the top row of Figure 6. Figure 6 also shows the mean ADC maps calculated from single-, two-, and four-shot experiments. The improvements in the images, particularly close to air–tissue interfaces, are evident with the number of increasing shots. The quantitative values exhibited by ADCs in all the maps are also similar.

Motion Compensation in Interleaved SPEN

As mentioned, the referenceless reconstruction algorithm has the potential to correct in-plane motion occurring between shots. Figure 7 shows this by presenting images arising from phantom and brain scan experiments, whose reconstructions were implemented using the algorithm in Figure 2 in the absence and presence of motion. The displacements before and after the phantom/brain movements are evident in these panels. Nonetheless, the final images that were reconstructed by relying on the motion correction and the referenceless reconstruction algorithms described earlier (Fig. 7d) showed no noticeable blurring and were comparable with the four-shot interleaved SPEN images that were acquired when no movements occurred (Fig. 7e).

DISCUSSION AND CONCLUSIONS

This study examined an approach extending single-shot hybrid SPEN, to multishot interleaved acquisitions. This option rescinds the original method's goal of collecting a full 2D image in one scan; on the other hand, in just a few scans, it can deliver higher resolution images that are endowed with better SNR and are less susceptible to distortions arising from heterogeneous magnetic fields. Similar benefits had been reported previously in multishot acquisitions relying on EPI; as in such instances,

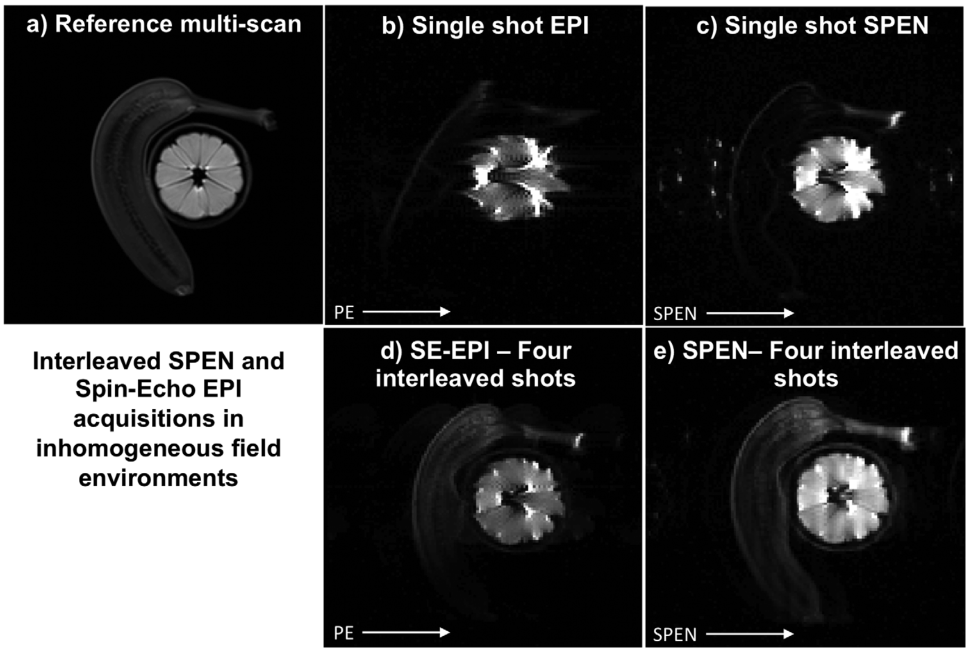

FIG. 4. Comparison of SE-EPI with SPEN in inhomogeneous field environments using a fruit setup with a banana and an orange. (**a**) Reference multiscan image. (**b**) Single-shot EPI image. (**c**) Single-shot SPEN image. (**d**) Interleaved four-shot SE-EPI image. (**e**) Interleaved four-shot SPEN image. Common scan parameters: FOV = $22 \times 22\,\text{cm}^2$, final resolution = $1.7 \times 1.7\,\text{mm}^2$, slice thickness = 5 mm. The four-shot SPEN used the sequence in Figure 1a with a flip angle = 60 deg, $T_{enc} = 24$ ms, $T_{acq} = 24$ ms, $G_{enc} = 0.05$ G/cm, TE = 7–55 ms, number of acquired points per shot = 128×33, and TR = 0.75 s. Parameters for the single-shot SPEN were: flip angle = 90 deg, $T_{enc} = 88$ ms, $T_{acq} = 88$ ms, $G_{enc} = 0.04$ G/cm, TE = 7–186 ms, number of acquired points = 128×128, and TR = 3 s. Parameters for the four-shot EPI were: flip angle = 60 deg, $T_{acq} = 24$ ms, TE = 30 ms, number of acquired points per shot = 128×33, and TR = 0.75 s. Parameters for the single-shot EPI were: flip angle = 90 deg, $T_{acq} = 88$ ms, TE = 94 ms, number of acquired points = 128×128, and TR = 3 s. Reference spin echo multiscan acquisitions were also collected using the following parameters: resolution = $0.93 \times 0.93\,\text{mm}^2$, TE = 72 ms, TR = 1.5 s, number of scan averages = 2, and total scan duration = 35 s.

much of the sensitivity and robustness gains of multishot SPEN derive from the use of progressively shorter echoes and acquisitions. In the case of interleaved multishot EPI, these potential benefits are often offset by the ensuing experiment's sensitivity to phase errors between shots, calling for a need for additional navigator scans or for double-FOV 2D reference scans. By contrast, an attractive feature of the interleaved multishot SPEN approach is the fact that all the information required for performing its phase error correction is "built into" the individual images that are combined. This allows one to reap the full benefits of interleaved schemes while obviating the need for collecting extra reference acquisitions. The robustness of the referenceless algorithm described herein is evidenced by its ability to correct even for the large phase errors arising when an object is purposefully moved between shots. Nonetheless, strip-like artifacts are visible in some of the illustrated images. These appear related to challenges in performing a perfect phase correction by the self-referenced SR algorithm; further research incorporating regularization methods as well as B_0 inhomogeneity corrections into the algorithm might alleviate these artifacts (47). In the present study, a somewhat simplistic approach was used to implement the individual images joint coregistration; more involved algorithms considering out-of-plane motions as well plastic deformations of the object could also be included (48). Accounting for such motion-derived distortions was found secondary in applications such as the fMRI study presented in Figure 5, where spontaneous instabilities dominated the intermittent phase variations between shots; however, they were relevant when analyzing other tissues in which involuntary motion is unavoidable (e.g., breast).

An important consideration in SPEN relates to the experiment's SAR, which tends to be higher than in EPI-based counterparts. To consider how SAR changes in multishot acquisitions, we recall that in SPEN sequences, immunity to B_0 inhomogeneities depends on the $\frac{M}{\lambda_{enc} BW \cdot T_{enc}}$ ratio; therefore, when comparing SAR in single-shot versus multishot SPEN acquisitions, it is reasonable to keep this ratio constant while using parameters fulfilling the fully refocused condition. Because the SAR of a pulse is proportional to $\int |B_1|^2\, dt/TR$ (where TR is the repetition time) and for a chirp pulse $B_1 \propto \sqrt{R}$ (12), it follows that $SAR \propto {}^{BW \cdot T_{enc}}\!/_{TR}$. This means that in multishot SPEN experiments, where the duration of the excitation and acquisition periods is reduced while the chirp's *BW* is kept constant, the SAR of each interleaved shot will be lower than that of a single scan collected at the same TR. On the other hand, if one were to use a repetition time of TR/N_{shot} for the multishot SPEN, the SAR per total image would become the same as in the single-shot acquisition. Nonetheless, SAR limitations remain, particularly when considering a multislice scheme such as the one introduced in Figure 1b. While interleaved multislice brain imaging examinations can be performed with

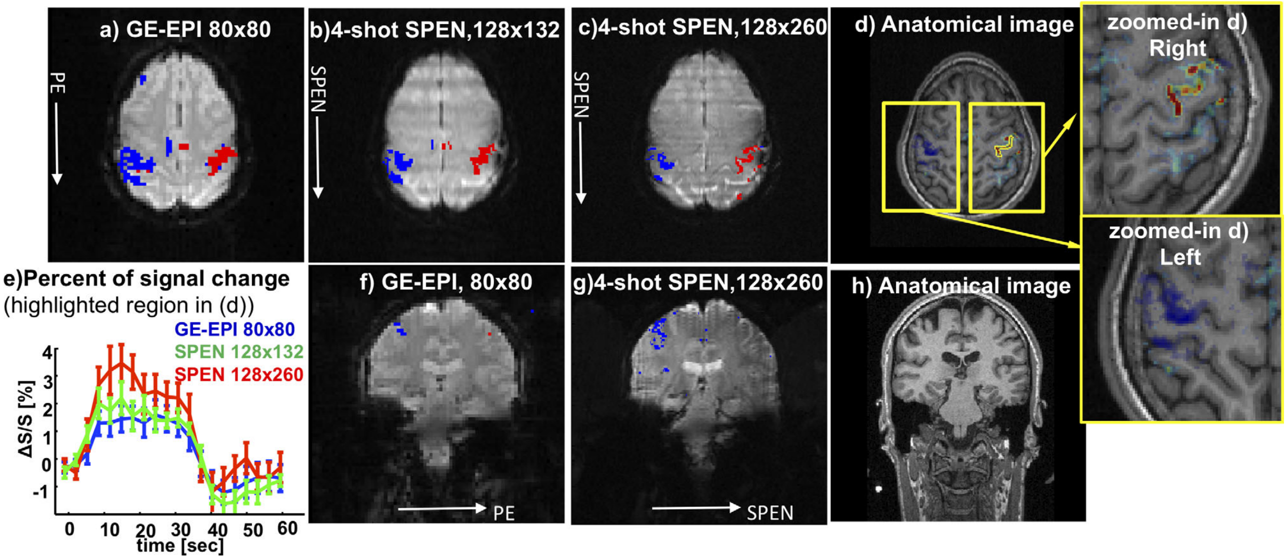

FIG. 5. fMRI results obtained upon applying finger tapping motor stimuli and monitoring with single-shot GE-EPI and interleaved four-shot SPEN. (**a–d**): Axially oriented experiments. (**f–h**): Coronal slice experiments. (a) Single-shot GE EPI scan acquisition with 80 × 80 pixels. (b) Interleaved SPEN acquisition with 128 × 132 pixels. (c) Interleaved four-shot SPEN acquisition with 128 × 260 pixels. (d) Axial anatomical image and magnifications showing the t-score maps overlay and, in yellow, the contour of an activated area that accurately follows the fine structure of the underlying gray matter anatomy, which was used for estimating the average percent signal changes in (e). (e) Percent signal activation for regions shown in yellow in (d). Three subjects underwent GE-EPI and 128 × 260-pixel SPEN experiments and one subject underwent 128 × 132-pixel SPEN; the standard errors in these plots were 0.55% for SPEN with 260 points, 0.40% for SPEN with 130 points, and 0.43% for GE-EPI (standard errors were calculated for the pixels in the region shown in yellow, and in equivalent regions in other subjects). (f–h) Analogous data, but for coronal experiments. The common scan parameters for these experiments were: FOV = 22 × 22 cm^2 and slice thickness = 5 mm. The single-shot GE-EPI parameters were: resolution = 2.75 × 2.75 mm^2, flip angle = 90 deg, T_{acq} = 56 ms, TE = 30 ms, number of acquired points = 80 × 80, and TR = 3 s. An interleaved set of four-shot SPEN experiments was also performed using the multislice 180 deg pulse-based sequence in Figure 1b with the following parameters: resolution = 1.7 × 1.7 mm^2, flip angle = 60 deg, T_{enc} = 12 ms, T_{acq} = 24 ms, G_{enc} = 0.03 G/cm, TE = 44–68 ms, τ = 30 ms, number of acquired points per shot = 128 × 33, and TR = 0.75 s. A second set relied on the same sequence but employed higher resolution parameters: resolution = 1.7 × 0.85 mm^2, flip angle = 60 deg, T_{enc} = 24 ms, T_{acq} = 48 ms, G_{enc} = 0.06 G/cm, TE = 56–104 ms, τ = 30 ms, number of acquired points per shot = 128 × 65, and TR = 0.75 s. For the relatively thick slices examined and large activation regions found, repeated examinations revealed that motional errors were not a particular concern in these experiments, thus they were not explicitly accounted for. Notice that due to differences in T_2 weighting, the images in Figures 5b and 5c have different contrasts and differ from the GE-EPI image containing mostly T_2^*-weighted contrast.

SPEN, current implementations are restricted to the acquisition of approximately 12 slices using TR = 3 s (Fig. 8). Acquisition of more slices is also possible at the expense of reducing the bandwidth of the encoding pulse (and hence risking an increase in the susceptibility distortions). Further research to improve interleaved SPEN's multislicing capabilities, for example using 2D pulses for simultaneous slice selection and spatiotemporal encoding (49), are in progress.

To evaluate the potential benefits derived from the interleaved procedure, two in vivo experiments that normally rely on EPI sequences were examined. One involved functional MRI measurements, and its aim was discerning the benefits that interleaved SPEN could provide in terms of image definition. Though simple, robust, and immune to motions, this approach may not always be suitable, as when the stimulus being followed consists of rapidly recurring cycles that are shorter than the duration required by the interleaved acquisitions. It is important to note that in SPEN-based implementations of fMRI and by variance to EPI, the image contrasts may differ for different spatial location. In the present study, T_2 weightings were spatially dependent, yet given the negligible contributions that T_2 effects had on the observed BOLD activation (essentially no activation could be observed upon working under fully refocused conditions for which T_2^* effects were cancelled), this did not introduce a severe functional penalty. The dominant BOLD contribution in the present study arose from breaking the fully refocused conditions ($T_{acq} = \lambda_{enc} T_{enc}$) by the introduction of a constant delay τ; this in turn afforded a uniform spatially sensitivity with regard to T_2^*, which as mentioned was the main source of the BOLD effects observed in these experiments. On the other hand, constant-time implementations of interleaved SPEN such as RASER (14,15) could provide uniform spatial contrast versus T_2 and T_2^*, provided that a constant T_2^*-encoding delay like the one used in this study is introduced. Other timing schemes can be conceived wherein neither T_2^* nor T_2 weights are spatially uniform. A full analysis involving these various fMRI scanning alternatives when implemented under the high-definition conditions illustrated in Figure 5 is in progress.

A second application examined the potential of fully refocused interleaved SPEN MRI for retrieving high-resolution diffusion-weighted images. While requiring

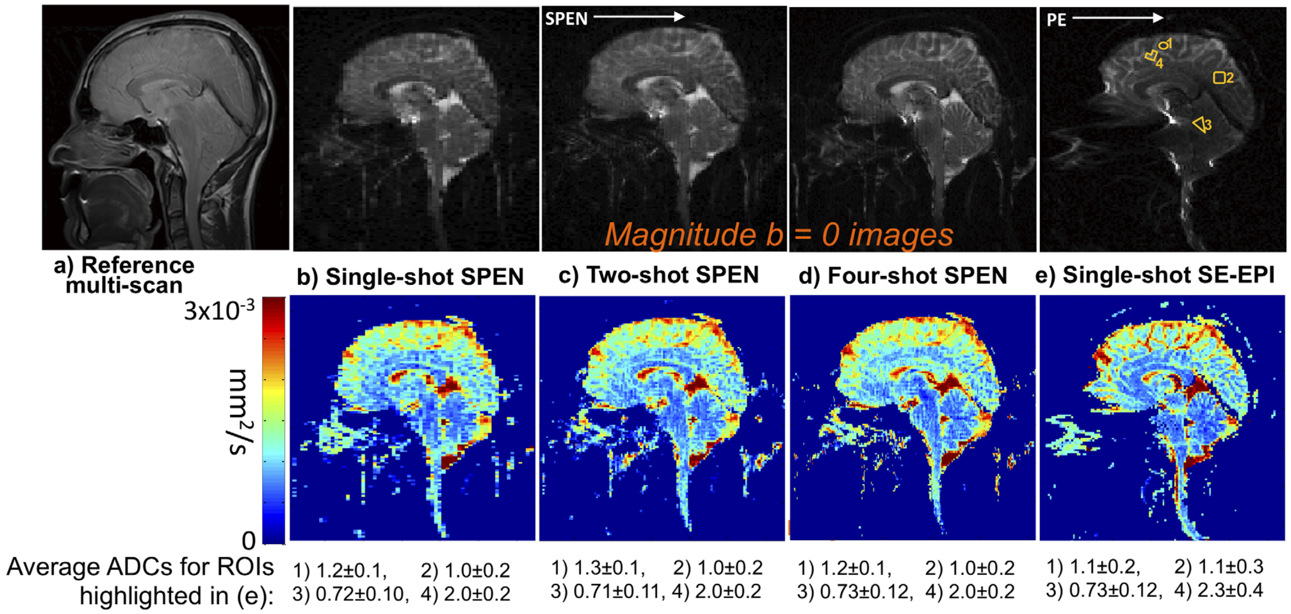

FIG. 6. Diffusion-weighted brain imaging results illustrating the b = 0 images arising from interleaved single-shot and multishot SPEN and EPI (top row), and the accompanying ADC maps resulting from multiple b-valued acquisitions collected on a single slice. (**a**) Reference multiscan image. (**b**) Low-resolution magnitude SPEN image reconstructed from a single scan. (**c**) Midresolution SPEN image reconstructed from two interleaved shots. (**d**) Four-shot interleaved SPEN image. (**e**) Single-shot SE-EPI imaging data. Interleaved SPEN parameters were: FOV = 24 × 24 cm^2, slice thickness = 5 mm, $N_{shot} = 4$, resolution = 1.87 × 0.9 mm^2, flip angle = 60 deg, $T_{enc} = 23$ ms, $T_{acq} = 45$ ms, $G_{enc} = 0.05$ G/cm, TE = 101–147 ms, number of acquired points per shot = 128 × 65, and TR = 0.75 s. SE-EPI scan parameters were: FOV = 24 × 24 cm^2, slice thickness = 5 mm, resolution = 1.87 × 1.87 mm^2, flip angle = 90 deg, $T_{acq} = 90$ ms, TE = 131 ms, number of acquired points = 128 × 128, and TR = 3 s. A spin echo multiscan reference was also acquired with: resolution = 0.6 × 0.6 mm^2, TE = 72 ms, TR = 1.5 s, average number of scans = 2, and total scan duration = 35 s. Indicated underneath each experiment are average ADC values obtained by each method for four generic regions defined in (e).

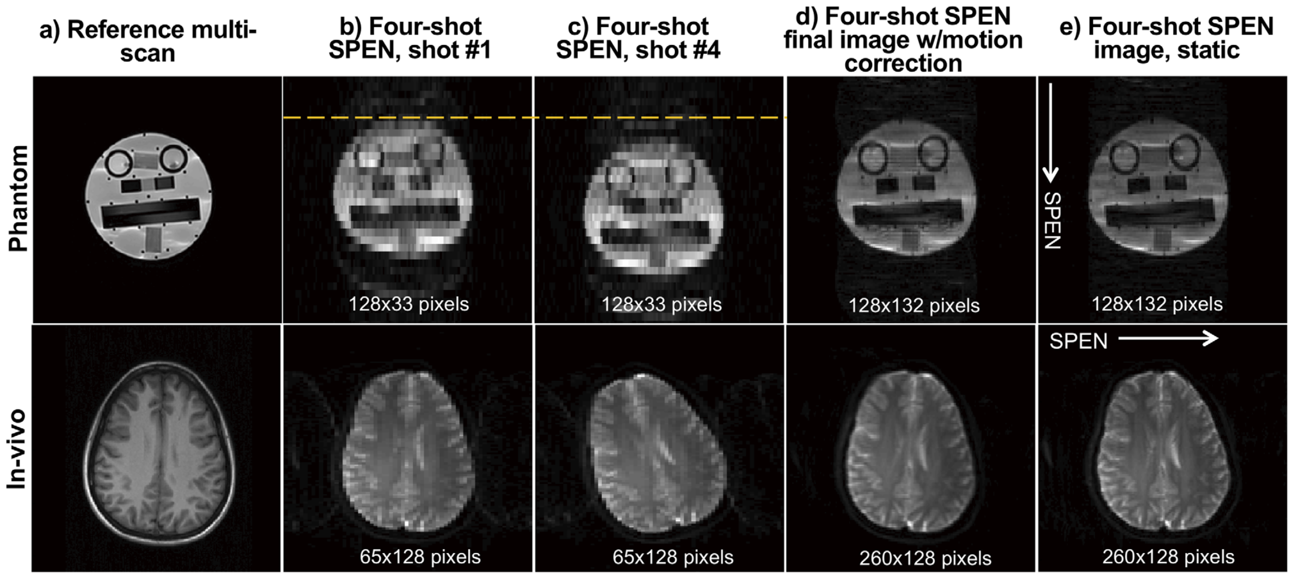

FIG. 7. Interleaved SPEN acquisitions incorporating the referenceless algorithm and a simple motion correction provision. Top row: Images arising from a manually moved phantom. Bottom row: Brain images arising from a volunteer who was asked to move his head side-to-side. (**a**) Reference multiscan image. (**b, c**) Separate initial and final shots collected as part of the interleaved SPEN set. The dashed yellow line highlights the extent of the movement. (**d**) Final interleaved image reconstructed in the case of movement from four scans. (**e**) Four-shot SPEN image reconstructed for a static case. Scanning parameters for these phantom motion experiments involved the SPEN sequence in Figure 1a with $N_{shot} = 4$, FOV = 16 × 16 cm^2, final resolution = 1.2 × 1.2 mm^2, slice thickness = 5 mm, flip angle = 60 deg, $T_{enc} = 30$ ms, $T_{acq} = 30$ ms, $G_{enc} = 0.1$ G/cm, TE = 7–67 ms, number of acquired points per shot = 128 × 33, and TR = 0.75 s. Multiscan spin echo images were also collected as reference with resolution = 0.93 × 0.93 mm^2, TE = 72 ms, TR = 1.5 s, 2 scan averages, total scan duration = 35 s. The parameters for the human brain in-plane rotations were: $N_{shot} = 4$, FOV = 24 × 24 cm^2, final resolution = 1.9 × 0.9 mm^2, slice thickness = 5 mm, flip angle = 60 deg, $T_{enc} = 24$ ms, $T_{acq} = 24$ ms, $G_{enc} = 0.03$ G/cm, TE = 7–55 ms, number of acquired points per shot = 128 × 65, and TR = 0.75 s. The reference multiscan parameters in this case were: resolution = 1 × 1 mm^2, flip angle = 9 deg, TE = 3 ms, TR = 2.3 s, and total scan duration = 4 min.

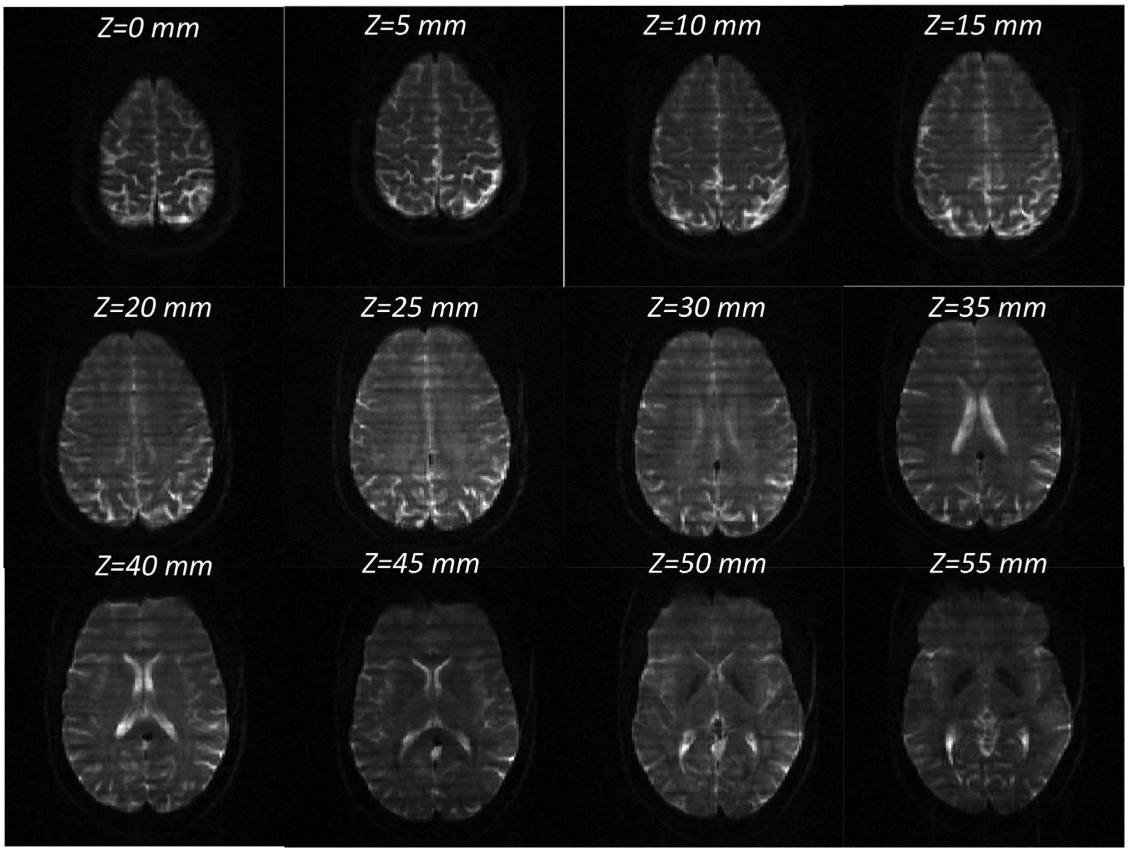

FIG. 8. Multislice four-shot SPEN brain images collected using the sequence illustrated in Figure 1b. Scan parameters were: number of slices = 12, resolution = 1.9 × 0.9 mm^2, flip angle = 90 deg, T_{enc} = 24 ms, T_{acq} = 48 ms, G_{enc} = 0.06 G/cm, TE = 30–78 ms, $\tau = 0$ ms, number of acquired points per shot = 128 × 65, and TR = 3 s.

some additional calculations with regard to their more usual *k*-based counterparts for deriving the exact b values needed (42), the results arising from these diffusion-weighted experiments are among the most promising aspects we envision for this interleaving method. Indeed, the ADC maps that were obtained yielded distributions that are quantitatively similar to their single-shot SE-EPI or SPEN counterparts, but with a considerably higher spatial resolution. This makes these experiments particularly promising alternatives for high-definition DTI or HARDI fiber tracking studies based on diffusion-weighted data (50,51), assuming that dense three-dimensional coverage can be provided. This is actually within the realm of the pulse sequence introduced in Figure 1b; Supporting Figure S1 presents multislice results conducted using such schemes, and interleaved DTI SPEN studies will be presented in an upcoming publication. Additional potential in vivo applications of this new fast form of imaging, including studies of flow and real-time motions as well as the incorporation of an additional spectral dimension, are currently under study.

APPENDIX

In addition to the formulations presented in the Theory section based on Ben-Eliezer et al. (37), this Appendix presents SNR aspects centering on 1) the effects of interleaving multishot acquisitions aiming to deliver similar data as a single-shot counterpart as a function of variable TRs and TEs for a variety of prototypical tissue T_1 and T_2 values and 2) potential blurring effects due to motion between the shots that could arise in interleaved SPEN acquisitions if not processed with the self-referenced SR algorithms described in this study.

SNR in multishot acquisitions can benefit from the significantly shortened echo times involved (21). This will provide higher immunity to B_0 inhomogeneities, as well as reduced T_2-derived losses that will usually overcompensate the SNR penalties associated to the interleaved scan's higher resolution. Nonetheless, some experiments (e.g., fMRI) might also seek to shorten the TR of the interleaved acquisitions to keep the total image collection time as short as in a single-shot imaging procedure. In such cases, the T_2-derived SNR gains achieved by shorter TEs will be partially reduced by saturation effects. In order to estimate how these various factors will affect interleaved SPEN's SNR, signals versus TE and TR were calculated for a range of relaxation parameters prototypical of gray and white matter tissues [$T_1 = 1.3$ s, $T_2 = 80$ ms for the former; $T_1 = 0.8$ s, $T_2 = 110$ ms for the latter (52)]. Figure A1 shows signal ratio maps for four-shot versus single-shot image acquisitions estimated from the spin echo steady-state signal intensity (53)

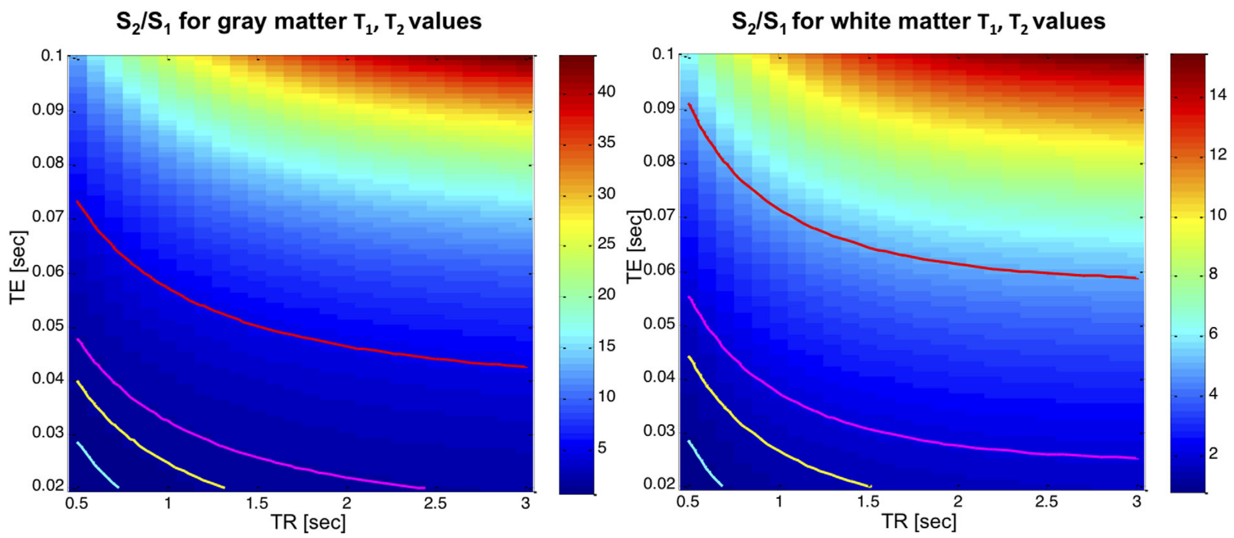

FIG. A1. Contour plots of the signal intensity ratios expected for four-shot interleaved (S_2) and single-shot SPEN (S_1) acquisitions, for a variety of TE and TR values. In a usual SPEN experiment, TE values (ie, T_2 weightings) will span the indicated range (20–100 ms), with the interleaved acquisition TEs being approximately four times shorter than their single-shot counterparts. As for TR, this was fixed at 3 s for the single-shot acquisition. The bottom axis ($0.5\ s \leq TR \leq 3\ s$) indicates the penalties introduced in the four-shot acquisition upon decreasing TRs. Left: Calculations for prototypical gray matter $T_1 = 1.3$ s, $T_2 = 80$ ms values. Right: Idem for white matter ($T_1 = 0.8$ s, $T_2 = 110$ ms). Contour lines are added for signal ratios equal 1, 1.5, 2, and 5 in cyan, yellow, magenta, and red.

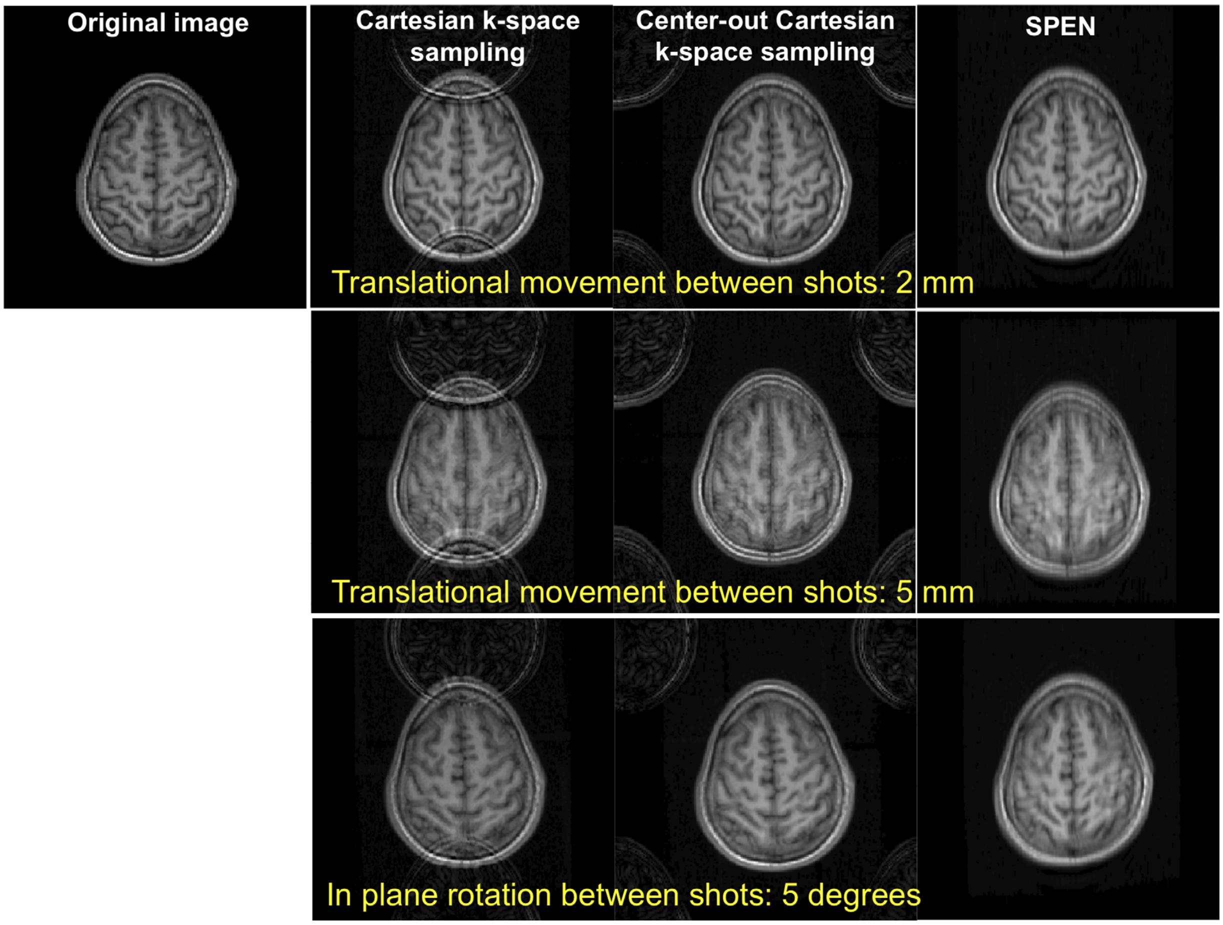

FIG. A2. Expected effects of different kinds of intershot movements. Left: Two-shot interleaved EPI performed with Cartesian sampling. Center: Two-shot interleaved EPI performed with center-out spiral sampling. Right: The interleaved SPEN sampling/processing introduced in this study. Motions included 2- and 5-mm translations along the low-bandwidth (phase-encoding for EPI and spatiotemporal-encoding direction for SPEN) dimensions, as well as a 5 deg in-plane rotation. The input used for these simulations is the T_1-weighted brain image shown in the upper left corner.

$$S_{steady-state} = M_0 \cdot \sin(\theta) \cdot e^{-TE/T_2} \cdot \frac{[1 + e^{-TR/T_1} - 2e^{(-TR/T_1 + TR/2T_1)}]}{[1 + e^{-TR/T_1} \cdot \cos(\theta)]}, \qquad [A1]$$

where M_0 is the initial magnetization and θ is the flip angle. The maps in Figure A1 show that in the relevant range of $40 \leq \mathrm{TE} \leq 100$ ms and for a $\mathrm{TR} = 0.75$ s as used in our experiments, the (spatially dependent) signal improvements will range between 2 and 20 for gray matter and between 2 and 9 for white matter (flip angles in these simulations were kept fixed to reduce the amount of variables changed simultaneously).

A second image-quality topic to consider in interleaved experiments relates to the potential artifacts that may arise due to motion between the shots. Cartesian-encoded EPI experiments will then evidence documented ghosting artifacts (22–25); if a spiral k-space encoding is used, these artifacts will be minimized and blurring effects will occur (54). If no precautions are taken, simulations reveal that—as in the latter spiral EPI case—interleaved multishot Cartesian SPEN acquisitions will be free from ghosting artifacts but will be subject to blurring (Fig. A2). On the other hand, if in these multishot SPEN experiments the segments are compatibilized by the self-referenced procedure introduced in this study prior to their SR reconstruction, these blurring effects are largely attenuated and all movement effects virtually eliminated. Overall, global phase errors occurring between shots due to in-plane motion can be well corrected by the algorithm; through-plane movements are not explicitly addressed by the algorithm, although we find that these are partially compensated when small, and their main effect is inducing a constant phase error (eg, due to inhomogeneity-induced B_0 changes).

ACKNOWLEDGMENTS

We thank Sagit Shushan (Wolfson Medical Center), Edna Haran, and the Weizmann MRI technician team for assistance in the human imaging scans.

REFERENCES

1. Mansfield P. Multi-planar image formation using NMR spin echoes. J Phys C Solid State Phys 1977;10:55–58.
2. Schmitt F, Stehling MK, Turner R. Echo-planar imaging: theory, technique and application. Berlin: Springer; 1998.
3. Edelman RR, Siewert B, Darby DG, Thangaraj V, Nobre AC, Mesulam MM, Warach S. Qualitative mapping of cerebral blood flow and functional localization with echo-planar MR imaging and signal targeting with alternating radio frequency. Radiology 1994;192:513–520.
4. Turner R, Jezzard P, Wen H, Kwong KK, Le Bihan D, Zeffiro T, Balaban RS. Functional mapping of the human visual cortex at 4 and 1.5 Tesla using deoxygenation contrast EPI. Magn Reson Med 1993; 29:277–279.
5. Bammer R, Keeling SL, Augustin M, Pruessmann KP, Wolf W, Stollberger R, Hartung HP, Fazekas F. Improved Diffusion-Weighted Single-Shot Echo-Planar Imaging (EPI) in Stroke Using Sensitivity Encoding (SENSE) Magn Reson Med 2001;46:548–554.
6. Cernicanu A, Lepetit-Coiffe M, Roland J, Becker CD, Terraz S. Validation of fast MR thermometry at 1.5 T with gradient-echo echo planar imaging sequences: phantom and clinical feasibility studies. NMR Biomed 2008;21:849–858.
7. Farzaneh F, Reidener SJ, Pelc NJ. Analysis of T2 limitations and off-resonance effects on spatial resolution and artifacts in echo-planar imaging. Magn Reson Med 1990;14:123–139.
8. Mishkovsky M, Frydman L. Principles and progress in ultrafast multidimensional nuclear magnetic resonance. Ann Rev Phys Chem 2009; 60:429–448.
9. Shrot Y, Frydman L. Spatially-encoded NMR and the acquisition of 2D magnetic resonance images within a single scan. J Magn Reson 2005;172:179–190.
10. Tal A, Frydman L. Spatial encoding and the acquisition of high definition MR images in inhomogeneous magnetic fields. J Magn Reson 2006;181:179–194.
11. Ben-Eliezer N, Shrot Y, Frydman L. High-definition single-scan 2D MRI in inhomogeneous fields using spatial encoding methods. Magn Reson Imaging 2010;28:77–86.
12. Tal A, Frydman L. Single-scan multidimensional magnetic resonance. Prog Nucl Magn Reson Spectrosc 2010;57:241–292.
13. Ben-Eliezer N, Frydman L. Spatiotemporal encoding as a robust basis for fast three-dimensional in vivo MRI. NMR Biomed 2011;24:1191–1201.
14. Chamberlain R, Park JY, Corum C, Yacoub E, Ugurbil K, Jack CR, Garwood M. RASER: a new ultrafast magnetic resonance imaging method. Magn Reson Med 2007;58:794–799.
15. Goerke U, Garwood M, Ugurbil K. Functional magnetic resonance imaging using RASER. Neuroimage 2011;54:350–360.
16. Solomon E, Avni R, Hadas R, Raz T, Garbow JR, Bendel P, Frydman L. Neeman M. Major mouse placental compartments revealed by diffusion-weighted MRI, contrast-enhanced MRI, and fluorescence imaging. Proc Natl Acad Sci U S A 2014;111:10353–10358.
17. Schmidt R, Frydman L. Alternative 1H MRI thermometry by single scan spatiotemporal encoding, Magn Reson Mater Phys 2013;26:477–490.
18. Cohen MS, Weisskoff RM. Ultra-fast imaging. Magn Reson Imaging 1991;9:1–37.
19. Butts K, Riederer SJ, Ehman RL, Thompson RM, Jack CR. Interleaved echo planar imaging on a standard MRI system. Magn Reson Med 1994;31;67–72.
20. Reeder SB, Atalar E, Bolster BD, McVeigh ER. Quantification and reduction of ghosting artifacts in interleaved echo-planar imaging. Magn Reson Med 1997;38:429–439.
21. McKinnon GC. Ultrafast interleaved gradient echo planar imaging on a standard scanner. Magn Reson Med 1993;30:609–616.
22. Noll DC, Schneider W. Theory, simulation, and compensation of physiological motion artifacts in functional MRI. Proc IEEE Int Conf Image Processing 1994;3:40–44.
23. Anderson AW, Gore JC. Analysis and correction of motion artifacts in diffusion weighted imaging. Magn Reson Med 1994;32:379–387.
24. Zeller M, Kraus P, Muller A, Bley TA, Kostler H. Respiration impacts phase difference-based field maps in echo planar imaging. Magn Reson Med 2014;72:446–451.
25. O'Halloran RL, Holdsworth S, Aksoy M, Bammer R. Model for the correction of motion-induced phase errors in multishot diffusion-weighted-MRI of the head: are cardiac-motion-induced phase errors reproducible from beat-to-beat? Magn Reson Med 2012;68:430–440.
26. Butts K, de Crespigny A, Pauly JM, Moseley M. Diffusion-weighted interleaved echo-planar imaging with a pair of orthogonal navigator echoes. Magn Reson Med 1996;35:763–770.
27. Wong EC. Shim insensitive phase correction for EPI using a two echo reference scan. Proc Intl Soc Magn Reson Med 1992;4514.
28. Liu C, Bammer R, Kim DH, Moseley ME. Self-navigated interleaved spiral (SNAILS): application to high-resolution diffusion tensor imaging. Magn Reson Med 2004;52:1388–1396.
29. Clare S. Iterative Nyquist ghost correction for single and multi-shot EPI using an entropy measure. Proc Intl Soc Mag Reson Med 2003; 11.
30. Seginer A, Schmidt R, Leftin A, Solomon E, Frydman L. Referenceless reconstruction of spatiotemporally encoded imaging data: principles and applications to real-time MRI. Magn Reson Med 2014;72: 1687–1695.
31. Kunz D. Use of frequency-modulated radiofrequency pulses in MR imaging experiments. Magn Reson Med 1986;3:377–384.
32. Pipe JG. Spatial encoding and reconstruction in MRI with quadratic phase profiles. Magn Reson Med 1995;33:24.
33. Ben-Eliezer N, Irani M, Frydman L. Super-resolved spatially-encoded single-scan 2D MRI. Magn Reson Med 2010;63:1594–1600.
34. Chen Y, Li J, Qu X, Chen L, Cai C, Cai S, Zhong J, Chen Z. Partial Fourier transform reconstruction for single-shot MRI with linear frequency-swept excitation. Magn Reson Med 2012;69:1326–1336.

35. Cai C, Dong J, Cai S, Li J, Chen Y, Bao L, Chen Z. An efficient deconvolution reconstruction method for spatiotemporal-encoding single-scan 2D MRI. J. Magn Reson 2013;228:136–147.
36. Schmidt R, Frydman L. New spatiotemporal approaches for fully-refocused, multi-slice ultrafast 3D MRI. Magn Reson Med 2013l 71: 711–722.
37. Ben-Eliezer N, Shrot Y, Frydman L, Sodickson DK. Parametric analysis of the spatial resolution and signal-to-noise ratio in super-resolved spatiotemporally encoded (SPEN) MRI. Magn Reson Med 2014;72:418–429.
38. Reeder SB, Atalar E, Faranesh AZ, McVeigh ER. Multi-echo segmented k-space imaging: an optimized hybrid sequence for ultrafast cardiac imaging. Magn Reson Med 1999;41:375–385.
39. Witt ST, Laird AR, Meyerand ME. Functional neuroimaging correlates of finger-tapping task variations: an ALE meta-analysis. NeuroImage 2008;42:343–356.
40. Hazewinkel M. Encyclopaedia of mathematics. Dordrecht: Kluwer Academic Publishers; 1993. 536 p.
41. Boynton GM, Engel SA, Glover GH, Heeger DJ. Linear systems analysis of functional magnetic resonance imaging in human V1. J Neurosci 1996;16:4207–4221.
42. Stejskal EO, Tanner JE. Spin diffusion measurements: spin echoes in the presence of a time-dependent field gradient. J Chem Phys 1965; 42:288–292.
43. Solomon E, Shemesh N, Frydman L. Diffusion weighted MRI by spatiotemporal encoding: analytical description and in vivo validations. J Magn Reson 2013;232:76–86.
44. Maier F, Fuentes D, Weinberg JS, Hazle JD, Stafford RJ. Robust phase unwrapping for MR temperature imaging using a magnitude-sorted list, multi-clustering algorithm. Magn Reson Med 2015;73: 1662–1668.
45. Vlachos M. Image registration. Scientific educational MATLAB database web site. http://m2matlabdb.ma.tum.de/download.jsp?MC_ID=12&SC_ID=18&MP_ID=389. Published November 08, 2005. Accessed January 1, 2014.
46. Lagarias JC, Reeds JA, Wright MH, Wright PE. Convergence properties of the Nelder-Mead simplex method in low dimensions, SIAM J Optim 1998;9:112–147.
47. Li J, Chen L, Cai S, Cai C, Zhong J, Chen Z. Imaging with referenceless distortion correction and flexible regions of interest using single-shot biaxial spatiotemporally encoded MRI. NeuroImage 2015;105:93–111.
48. Wang Y, Ehman RL. Retrospective adaptive motion correction for navigator-gated 3D coronary MR angiography. J Magn Reson Imaging 2000;11:208–214.
49. Schmidt R, Frydman L. Multi-slice ultrafast spatiotemporal encoding (SPEN) MRI by new two dimensional excitation pulses. Proc Intl Soc Mag Reson Med 2014;22:1439.
50. Basser PJ, Pierpaoli C. Microstructural and physiological features of tissues elucidated by quantitative-diffusion-tensor MRI. J Magn Reson 1996;111:209–219.
51. Tuch DS, Reese TG, Wiegell MR, Makris N, Belliveau JW, Wedeen VJ. High angular resolution diffusion imaging reveals intravoxel white matter fiber heterogeneity. Magn Reson Med 2002;48:577–582.
52. Wansapura JP, Holland SK, Scott Dunn R, Ball WS. NMR relaxation times in the human brain at 3.0 Tesla. J Magn Reson Imaging 1999;9: 531–538.
53. Kuperman V. Magnetic resonance imaging: physical principles and applications. San Diego: Academic Press; 2000.
54. Bernstein MA, King KF, Zhou XJ. Handbook of MRI pulse sequences. Elsevier: Academic Press; 2004.

SUPPORTING INFORMATION

Additional Supporting Information may be found in the online version of this article.

Figure S1. Multislice breast volunteer imaging comparing four-shot interleaved SE-EPI and SPEN acquisitions for seven slices chosen as well as for a reference multiscan acquisition. Both the EPI and the SPEN experiments were executed with fat suppression; the latter set exploited SPEN's zooming abilities along the low-bandwidth (vertical) dimension. Interleaved SPEN parameters were as follows: FOV = 28 × 14 cm^2, slice thickness = 5 mm, $N_{\text{shot}} = 4$, resolution = 1.7 × 0.85 mm^2, flip angle = 60°, $T_{\text{enc}} = 15$ ms, $T_{\text{acq}} = 30$ ms, $G_{\text{enc}} = 0.05$ G/cm, TE = 40–70 ms, number of acquired points per shot = 160 × 41, and TR = 3 s. Interleaved four-shot EPI parameters: FOV = 28 × 28 cm^2, slice thickness = 5 mm, $N_{\text{shot}} = 4$, resolution = 1.45 × 1.45 mm^2, flip angle = 60°, G/cm, TE = 44 ms, number of acquired points per shot = 192 × 49, and TR = 3 s. A spin echo multiscan reference was also acquired with resolution = 1.4 × 1.4 mm^2, TE = 72 ms, TR = 1.5 s, scans averaged = 2, total scan duration = 35 s.

Figure S2. Interleaved multishot SPEN imaging (collected with T_2^* weighting for the sake of eventual fMRI), acquired for the same slice of a brain volunteer in four independent sets of experiments. For each set of experiments, data rows show the following data: magnitude images of the four individual shots; phase differences $\Delta\varphi$ between two pairs –{1,3} and {2,4}– of consecutive shots; two midresolution images arising for each of these pairs upon performing the procedure in Figure 2; the phase differences between these midresolution images; and the final image coming from the latter's joint processing. The phase maps were fitted by a second-order polynomial and are shown multiplied by a mask to filter out noisy areas. Notice the relatively random behavior of these phase maps for individual experimental sets.